Bispectrum speckle interferometry of the massive protostellar outflow source IRAS 23151+5912[*]

G. Weigelt[1], H. Beuther[2], K.-H. Hofmann[1], M.R. Meyer[3], Th. Preibisch[1], D. Schertl[1], M.D. Smith[4], and E.T. Young[3]

[1] Max-Planck-Institut für Radioastronomie, Auf dem Hügel 69, D–53121 Bonn, Germany
[2] Harvard-Smithsonian Center for Astrophysics, 60 Garden Street, Cambridge, MA 02138, USA
[3] Steward Observatory, University of Arizona, 933 North Cherry Avenue, Tucson, AZ 85721, USA
[4] Armagh Observatory, College Hill, Armagh BT61 9DG, Northern Ireland

Abstract. We present bispectrum speckle interferometry of the massive protostellar object IRAS 23151+5912 in the near-infrared K' band. The reconstructed image shows the diffuse nebulosity north-east of two point-like sources in unprecedented detail. The comparison of our near-infrared image with mm continuum and CO molecular line maps shows that the brighter of the two point sources lies near the center of the mm peak, indicating that it is a high-mass protostar. The nebulosity coincides with the blue-shifted molecular outflow component. The most prominent feature in the nebulosity is a bow-shock-like arc. We assume that this feature is associated with a precessing jet which has created an inward-pointed cone in the swept-up material. We present numerical jet simulations that reproduce this and several other features observed in our speckle image of the nebulosity. Our data also reveal a linear structure connecting the central point source to the extended diffuse nebulosity. This feature may represent the innermost part of a jet that drives the strong molecular outflow (PA $\sim 80°$) from IRAS 23151+5912. With the aid of radiative transfer calculations, we demonstrate that, in general, the observed inner structures of the circumstellar material surrounding high-mass stars are strongly influenced by the orientation and symmetry of the bipolar cavity.

Key words. techniques: interferometric – stars: individual: IRAS 23151+5912 – stars: formation – stars: outflows

1. Introduction

The formation of massive stars is usually associated with strong outflow activity. In fact, many massive protostars have been identified by their massive molecular outflows observed at radio wavelengths. These outflows seem to be an essential ingredient of the star formation process (for a review see, e.g., Reipurth & Bally 2001) as they are believed to contribute to the removal of excess angular momentum from accreted matter and to disperse infalling circumstellar envelopes. Despite their key role in star formation, the origin, acceleration, and collimation of the flows are still poorly understood, mainly because these processes are believed to occur on very small spatial scales. This clearly demonstrates the need for high spatial-resolution studies in order to reach a better understanding of the star-formation process.

For low-mass young stellar objects (YSOs), many observations have indicated that the molecular outflows are momentum-driven by protostellar jets, which entrain the surrounding material. In the formation of high-mass stars, it is unclear whether we simply see a scaled-up version of the processes working in low-mass objects or whether there are fundamental differences between the high- and low-mass star formation regimes. It has often been argued that the outflows from high-mass protostars generally display a considerably more complex structure and are less collimated than outflows from low-mass YSOs, suggesting fundamental differences. Alternative outflow driving mechanisms for massive YSOs include the deflection of accreted material (Churchwell 2000) and the strong winds of hot, massive stars (e.g. Devine et al. 1999).

Beuther et al. (2002a) studied the bipolar outflows in a large sample of high-mass star-forming regions. They found generally continuous correlations of the outflow properties from the low-mass to the high-mass regime, suggesting a common mechanism for the origin of the outflows for all masses. Their mm data are consistent with massive outflows being as collimated as their low-mass counterparts.

High spatial-resolution imaging of the inner circumstellar environment in YSOs can shed light on the origin

---

of the flows and the mechanism responsible for the initial collimation of the beams. Studies with the HST, adaptive optics, and infrared long-baseline interferometry have recently yielded important information on the inner circumstellar environment of many YSOs (e.g. Stapelfeldt et al. 1998; Brandner et al. 2000; Millan-Gabet & Monnier 2002; Leinert et al. 2004; Eisner et al. 2005; Akeson et al. 2005) and have revealed spectacular manifestations of the interaction of the jets and outflows with the surrounding material (e.g. Dougados et al. 2000). Bispectrum speckle interferometry has revealed inner circumstellar structures of very complex morphology around several massive and intermediate-mass YSOs (e.g., Schertl et al. 2000; Weigelt et al. 2002ab; Preibisch et al. 2001, 2002, 2003; Hofmann et al. 2004). These results were the motivation for our speckle interferometric study of the YSO IRAS 23151+5912 presented in this paper. If we can distinguish infalling envelope material from outflows surrounding massive stars, we will gain insight into: 1) whether the relationship between mass accretion and mass loss for low-mass stars also applies to higher mass protostars; 2) the injection of kinetic energy into molecular cloud cores from the formation of massive stars; and 3) the effects that outflows might have on the emergent initial mass function in massive star-forming regions. Our long-term program attempts to answer these questions with a systematic study of massive protostars at high angular resolution utilizing the techniques of bispectrum speckle interferometry.

The infrared source IRAS 23151+5912 is located in a rather isolated molecular cloud in the Cepheus region to the south of the HII region Sh2-157. The IRAS fluxes show a strongly rising broad-band spectrum with a peak at $60\,\mu m$, demonstrating the presence of large amounts of warm dust. The ISO SWS spectrum rises very steeply between $4\,\mu m$ and $45\,\mu m$ and shows a deep and broad silicate absorption feature around $10\,\mu m$. The ISOPHOT spectrum shows another strong absorption feature at $3\,\mu m$, which can be explained by ice mantles on the dust grains. These two absorption features suggest that the central source is deeply embedded in dense circumstellar material.

While IRAS 23151+5912 is completely invisible at optical wavelengths, it is a bright object in the near-infrared K band. The K-band image by Hodapp (1994; seeing-limited resolution of $\sim 1''$) shows two point sources and a diffuse nebula. A near-infrared imaging ($\sim 1.8''$ resolution) and spectroscopic study of IRAS 23151+5912 and its surroundings was recently presented by Chen & Yao (2004).

A bipolar molecular outflow from IRAS 23151+5912 was detected in the CO observation by Wouterloot et al. (1989). IRAS 23151+5912 is part of a large sample of 69 very young high-mass star-forming regions intensely studied by Sridharan et al. (2002) and Beuther et al. (2002a,b,c). We will use the source parameters listed in Beuther et al. (2002b). The source is at a distance of

$\sim 5.7\,\mathrm{kpc}$ with a bolometric luminosity of $10^5\,L_\odot$, suggesting a mass of about $25\,M_\odot$ for the YSO. The source exhibits a massive bipolar outflow in the east-west direction; the direction of the line connecting the peaks of the red- and blue-shifted CO maps is along position angle PA = 79°. The masses of the red and blue outflow lobes are $\sim 8\,M_\odot$ and $\sim 13\,M_\odot$, respectively. The size of the outflow system is 0.55 pc and the collimation factor (i.e. the ratio of the length to the width of the flow) is 1.2. Note that this relatively small collimation factor does not necessarily imply that the outflow is poorly collimated, since this value strongly depends on the beam size and the inclination angle (which is probably quite large). The dynamical age of the outflow is estimated to be only 20 000 years.

Wouterloot & Walmsley (1986), Scalise et al. (1989), Felli et al. (1992), Tofani et al. (1995), and Beuther et al.(2002c) detected H_2O maser emission in IRAS 23151+5912. The presence of these masers is an additional signpost of the youth of this object. Furthermore, the non-detection of IRAS 23151+5912 at 3.6 cm with the VLA at a 1 mJy sensitivity limit indicates that the object is in a very early evolutionary stage prior to forming a significant ultracompact H II region.

2. Observations and data analysis

The speckle interferograms of IRAS 23151+5912 were recorded on 20 December 2004 with the 6.5 m MMT in Arizona. The detector of our speckle camera was a Rockwell HAWAII array (only one 512×512 quadrant was used). The size of one pixel corresponds to 27.0 mas on the sky. A K-band filter with central wavelength 2115 nm and bandwidth 214 nm was used. This filter bandwidth includes the 1-0 S(1) emission line of molecular hydrogen at $2.12\,\mu m$ and and the Br γ line. The speckle interferograms of the unresolved star HD 240212 were used for the compensation of the atmospheric speckle transfer function. The exposure time per frame was 590 ms. Our data set consists of 350 speckle interferograms of IRAS 23151+5912 and 150 speckle interferograms of the unresolved reference star HD 240212. The field-of-view was $11.3'' \times 11.3''$. The seeing (FWHM) was $\sim 0.9''$.

The modulus of the Fourier transform of the object (visibility) was obtained with the speckle interferometry method (Labeyrie 1970). An image with a resolution of 320 mas (Fig. 1) was reconstructed from the data set using the bispectrum speckle interferometry method (Weigelt 1977; Weigelt & Wirnitzer 1983; Lohmann et al. 1983; Hofmann & Weigelt 1986).

3. Results

Our 320 mas resolution speckle reconstruction of IRAS 23151+5912 is presented in Fig. 1. Our image shows two point-like sources and extended diffuse nebulosity. We denote the point-like sources as IRS 1 (the brighter, northern object) and IRS 2. The distance between IRS 1 and IRS 2 is $3.6''$. Both objects appear
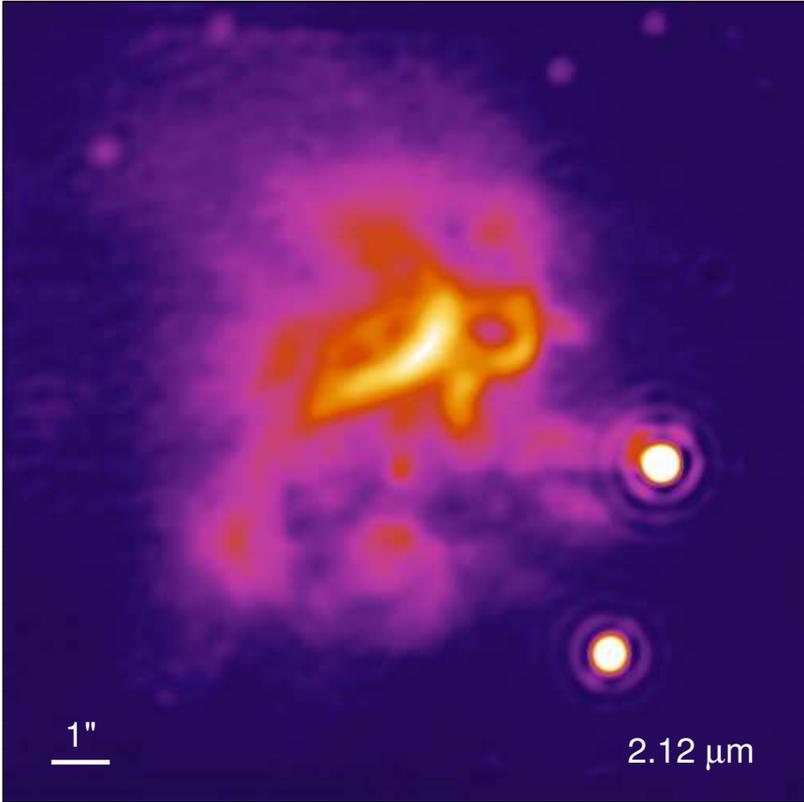
Fig. 1. Pseudocolor representation of our K'-band image of IRAS 23151+5912, reconstructed using the bispectrum speckle interferometry method. The field of view is $\sim 11'' \times 11''$. North is up, and east is to the left. We denote the upper of the two bright point-like sources in the lower right image quadrant as IRS 1, the lower one as IRS 2.
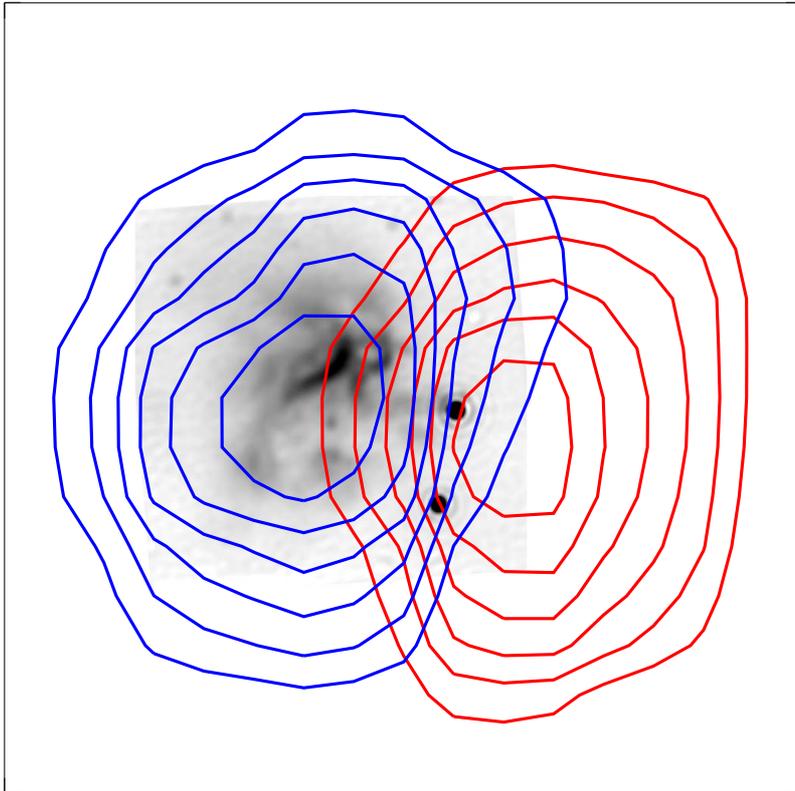

Fig. 2. Comparison of our K'-band speckle image of IRAS 23151+5912 (greyscale image) to the CO line maps from Beuther et al. (2002b) shown as red and blue contours for the red- and blue-shifted CO emission. The field-of-view is $30'' \times 30''$.

unresolved at the resolution of our image. The ratio of the fluxes of IRS 1 and IRS 2 is 1.53:1.

The total flux in our image is dominated by the diffuse nebulosity. By measuring the fluxes of IRS 1 and IRS 2 in $0.8''$ diameter apertures, we find that IRS 1 contributes just 5.6% to the total flux in the image, and IRS 2 only 3.7%. This means that 90.7% of the total flux in our $11'' \times 11''$ image comes from the extended nebula.

Comparison of our speckle image with the images from Hodapp (1994), the 2MASS images, and

the 2MASS All-Sky Catalog of Point Sources suggests that IRS 1 corresponds to 2MASS J23172102+5928480, while the peak of the diffuse nebulosity corresponds to 2MASS J231721.57+5928496. IRS 2 was not resolved as a separate point source in the 2MASS images. A comparison to the $\sim 1.8''$ resolution seeing-limited images from Chen & Yao (2004) suggests that IRS 1 corresponds to their source NIRS 34, while IRS 2 corresponds to their NIRS 35. Their source NIRS 19, which they regarded as the brightest "point source" and thus most massive "star" in IRAS 23151+5912, corresponds to the nebulous emission, which is completely resolved in our image. The fact that NIRS 19 is no stellar point source but apparently pure nebulosity also explains the colors of $H - K' = 1.3$ and $J - H = 3.3$ derived by Chen & Yao (2004), which place the source in the "forbidden" region of the $H - K'$ versus $J - H$ color-color diagram (i.e. to the left of the reddening band for photospheric colors; see their Fig. 3). These colors are consistent with the idea that a considerable fraction of the nebulous emission is scattered light.

3.1. Structure of the diffuse nebulosity

The nebulosity in the eastern part of our image shows a remarkable wealth of detail. Its structure is dominated by several curved features which look like bow shocks. Such bow shocks are seen in many young jet and outflow sources and can usually be interpreted as either the leading edge of jet-like streams of outflowing material or internal working surfaces within the jet flows. In remarkable contrast to "usual" bow-shocks, which are well aligned and point away from the jet source, the curved features in IRAS 23151+5912 appear to be oriented in random directions.

The nebulosity seems to be connected to IRS 1, but not to IRS 2. Considering the fainter parts of the nebula, as seen in the deep seeing-limited K-band image in Hodapp (1994), the shape of the nebula is clearly cone-like, with IRS 1 at its tip. The axis of the cone is along position angle PA $\sim 70° - 80°$ (similar to the PA of $\sim 80°$ of the CO outflow), and the opening angle is about $90°$. We also note that this deeper image shows several extended "finger"-like features that also clearly point to IRS 1; these features extend $\sim 20''$ outward at position angles of $\sim 120° - 140°$. IRS 2 appears to be outside the cone-like nebular structure and separated from the nebulosity.

Another very interesting feature is a narrow, elongated structure that seems to extend from IRS 1 to the nebulosity. The PA of this feature is $\sim 88°$. It displays a clumpy structure, with the brightest knot being located $2.0''$ from IRS 1. The width at this knot is $\sim 1.0''$ FWHM.

3.2. Comparison of the near-infrared emission to the mm maps

The detailed mm maps of IRAS 23151+5912 presented by Beuther et al. (2002b) (beam size $11''$) provide an op-

portunity to investigate the spatial relation between the observed near-infrared emission, the 1.2 mm emission, and the CO outflow structure. For the alignment of the various images, we used the nominal telescope pointing position for the mm maps to establish the coordinate system. Since the near-infrared source IRS 1 can be identified with 2MASS J23172102+5928480, we used its 2MASS position to align our speckle image with the mm maps. This alignment places IRS 1 into the central peak of the 1.2 mm continuum map and just between the red- and blue-shifted CO map peaks. In Fig. 2 we have plotted the contours of the red- and blueshifted mm emission over our K'-band speckle image. The comparison suggests that the diffuse nebulosity coincides very well with the peak of the blue-shifted CO emission. We note that the astrometric uncertainties of this comparison are significant. The positional uncertainty of the mm data (i.e. the possible pointing error) is $\leq 5''$, and due to the diffuse appearance of the near-infrared sources in the 2MASS images, we estimate the uncertainty of the 2MASS position of IRS 1 to be $\sim 1''$. Therefore, the formal uncertainty of our astrometric comparison does not allow us to fully prove that IRS 1 is actually in the center of the mm peak. However, for the reasons discussed below, we believe that IRS 1 is actually well centered in the cloud core.

4. Interpretation

4.1. Is IRS 1 the massive protostar in IRAS 23151+5912?

Many jet and outflow sources are so deeply embedded in their surrounding molecular cloud material that they are invisible in the near-infrared and can only be seen at longer wavelengths. It is therefore not immediately clear that IRS 1 is the massive protostar responsible for most of the infrared emission in IRAS 23151+5912. It may be an unrelated object, seen near the nebulosity by chance. However, there are a number of arguments suggesting that IRS 1 is, in fact, the near-infrared counterpart of the massive protostar driving the outflow:

First, we note that the 1.2 mm emission is very compact with a size of $16.5'' \times 14.4''$ (FWHM, measured in the mm-map with $11''$ beam size). The mm map, as well as all available mid- and far-infrared images, is consistent with the presence of a single, unresolved point source.

Second, the recent high-resolution mid-infrared study of IRAS 23151+5912 by Campbell et al. (2003) suggested the presence of a single unresolved point source. In their $10 \, \mu m$ and $20 \, \mu m$ images with a spatial resolution of $\sim 1.5''$, they found only a single point-like source in the center of the mm peak and derived a FWHM of $1.3''$ at $10 \, \mu m$ and $1.7''$ at $20 \, \mu m$. They also found that a major part of the mid-infrared emission comes from this point source. These results clearly suggest a single dominant source in the molecular cloud core, and it is very likely that the mid-infrared point source is identical to the mas-

sive protostar IRS 1. IRS 2 is not detected in these mid-infrared images.

Third, the very close proximity (angular separation $< 2''$) of IRS 1 to the H_2O masers found by Tofani et al. (1995) also suggests that IRS 1 is the protostar driving the outflow.

Finally, since our comparison of the speckle image with the radio maps also places IRS 1 at the center of the mm peak, and since deeper near-infrared images show no additional sources within $10''$ of IRS 1 and IRS 2, we believe that IRS 1 is identical to the mid-infrared source and, therefore, also to the massive protostar.

Further support for our assumption comes from the fact that IRS 1 lies at the tip of the cone-like nebulosity, and that the direction from IRS 1 to the nebulosity (PA $\sim$ 73°) agrees well with the CO outflow direction (PA = 79°). The presence of the jet-like structure connecting IRS 1 to the diffuse nebulosity also suggest a physical relation.

4.2. Relation of the near-infrared nebula to the outflow structure

The positional coincidence of the point-like source IRS 1 with the center of the mm emission and the diffuse near-infrared nebulosity with the blue-shifted CO emission peak suggests the following interpretation of the observed structures: the bright, point-like K-band source is the protostar in the center of the compact molecular cloud core. The protostar is embedded in a dense circumstellar envelope or perhaps a thick circumstellar disk. The outflow has cleared a cavity in the circumstellar material, and what we see as the diffuse nebulosity in our K'-band image is a combination of light from the central protostar that is scattered at the inner wall of this low-density outflow cavity or by material within the cavity in our direction, and of $2.12\,\mu m$ emission from shock-excited molecular hydrogen in the outflow. This interpretation is supported by the K-band spectrum of the peak of the nebulosity presented by Chen & Yao (2004), which shows strong emission in the $2.12\,\mu m$ H_2 line.

The asymmetric general shape of our image, i.e. the fact that we do not see a counter lobe to the west of IRS 1, is easily explained as a geometrical effect. The red-shifted outflow component has probably cleared a similar cavity, which is, however, much fainter and essentially invisible in our near-infrared image, because it is pointing away from us. In fact, the deep K-band image from Hodapp (1994) reveals a faint indication of the counter lobe to the west of IRS 1. The continuum subtracted $2.12\,\mu m$ H_2 line image from Chen & Yao (2004) also shows faint H_2 emission to the west of IRS 1.

4.3. Numerical simulations of a jet-driven outflow

We attempt here to model the observed nebula features in IRAS 23151+5912 more closely and interpret them in the context of an outflow driven by a jet precessing through a wide angle. In particular, we try to explain the prominent backward facing bow-shock like feature in the center of the nebulosity. For this purpose we performed three-dimensional hydrodynamic simulations that take a heavy molecular jet which cuts through a uniform external cloud, destroying some of the molecules in its path. In the fast precessing case, a reverse bow forms around the precession axis, from which the outflow is deflected (Rosen & Smith 2004b). This causes the outflow to be indented along the flow axis. In contrast, we note that jets with slow precession are shown to produce long curved streamers or multiple bow shocks rather than reverse bows (Smith & Rosen 2005).

Therefore, to determine if the observed strongly curved structures can be better simulated, we revised the input parameters as follows. We suspected that the features observed in IRAS 23151+5912 might correspond to an outflow driven by a jet with an *intermediate precession rate.* Clearly, we need a more specific definition of fast and slow precession rates by comparing the rotation speed with the outflow expansion speed. That is, the precession is fast if the precession period is smaller than the outflow expansion time. The latter is proportional to both the jet dynamical time scale $t_j = r_j/v_j$ and the ratio of jet to ambient density, $\eta = \rho_j/\rho_a$. It is also inversely proportional to $\sin\theta$ where θ is the half-angle of the precession cone, and r_j and v_j are the initial jet radius and speed (Smith & Rosen 2005).

Following published simulations, we took $v_j = 100$ km s^{-1}, $r_j = 1.7 \times 10^{15}$ cm, $\theta = 20°$ and $\eta = 10$. This yields an outflow expansion timescale of $\eta t_j/\sin\theta = 158$ yr. For comparison, published fast-precession simulations assumed a 50 year period while slow-precession runs took a 400 year period.

Hence, we here took a 150 year period. The resulting H_2 simulation reproduced the majority of the observed near-infrared features at the time of 248 yr after the launch of the jet (Fig. 3). The brightness distribution, however, does not entirely correspond, as discussed below.

Note that in the figure, the jet enters from a precessing nozzle on the right of the panel. The leading edge of the reverse bow (marked as A) has reached a distance of 5×10^{16} cm from the nozzle. In the observation, the edge of the bow is $\sim 6''$ from the driving star. At a distance of 5.7 kpc, this is an extent of 5×10^{17} cm, considerably larger than in the simulations. This implies that the simulation time scales should be scaled by a factor of 10 upwards, assuming a similar jet speed, to give a precession period of 1,500 yr and a source age of 2,500 yr. The lower panel of Fig. 3 displays the molecular hydrogen image convolved with a Gaussian beam with a standard deviation of 6. When scaled up to the observations of the source, this corresponds to about $0.15''$ and produces structure close to that of the speckle image.

How can this specific feature, so similar to the one observed, be found associated with a jet flow into a uniform density medium? Part of the answer lies in the intermediate precession period which allows the jet material to
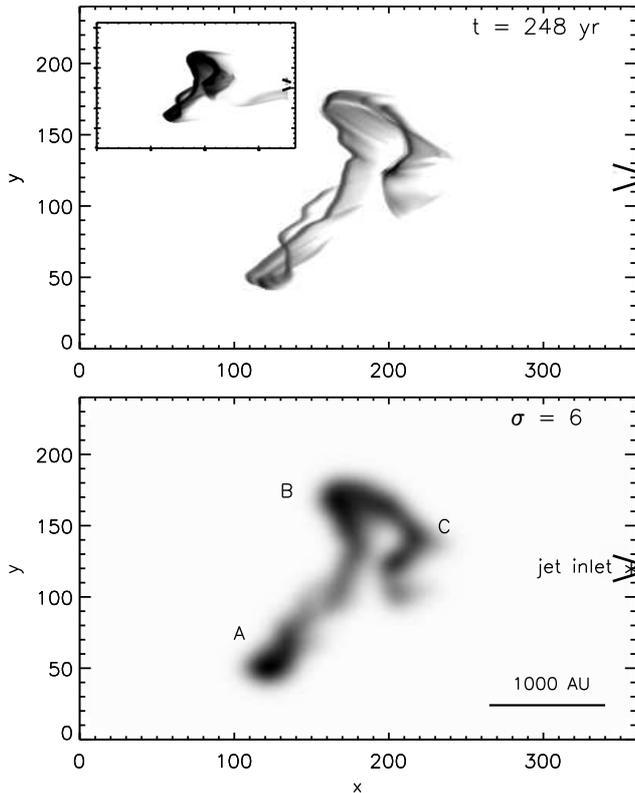
Fig. 3. Simulated images of the outflow resulting from a precessing jet of intermediate precession rate. The calculation was performed with a modified ZEUS-3D code on a grid of size $360 \times 240 \times 240$ zones. Each zone has a size of 2×10^{14} cm. Shown here are the 1-0 S(1) emission from H_2 at 2.12μm at the full numerical resolution (upper panel) and convolved with a Gaussian with $\sigma = 6$ zones (lower panel). The insert shows the appearance of a wispy jet feature on an 'over exposed' simulated image. The ambient medium begins with a uniform density of 10^4 cm^{-3} and the jet possesses a density of 10^5 cm^{-3} and a speed of 100 km s^{-1}. The jet speed was varied by superimposing ten per cent sinusoidal pulsations with a period of 60 yr. No shear was applied. Full details of the simulations can be found in Rosen & Smith (2004ab). Note that the view presented takes the axis about which the jet is precessing to be in the plane of the sky and the H_2 emission to be optically thin.

Fig. 4. CO J=2-1 emission at 230 GHz predicted from the simulation presented in Fig. 3. Only the CO which has been entrained (i.e. set in motion) is included in the image (i.e. the background cloud has been subtracted). The lower panel demonstrates the structure which would be detected when observed at low spatial resolution. The inset panel is an over-exposed simulation.

sweep out an arc-shaped shock into the ambient medium rather than a bow shock. However, although the jet is dense, the change in direction implies that the jet momentum is spread out over the same arc. Consequently, the ambient medium is able to provide resistance to the advancing jet and distort the shape of the arc. In addition, ten per cent perturbations to the magnitude of the jet speed have been superimposed which accelerate the distortion of the filamentary shock.

The simulated CO structure for the same execution is displayed in Fig. 4. Note that the leading edge is indented even when convolved, as seen in the observations, although only just perceptible. However, all other structure is smeared out. The dynamical time derived from the
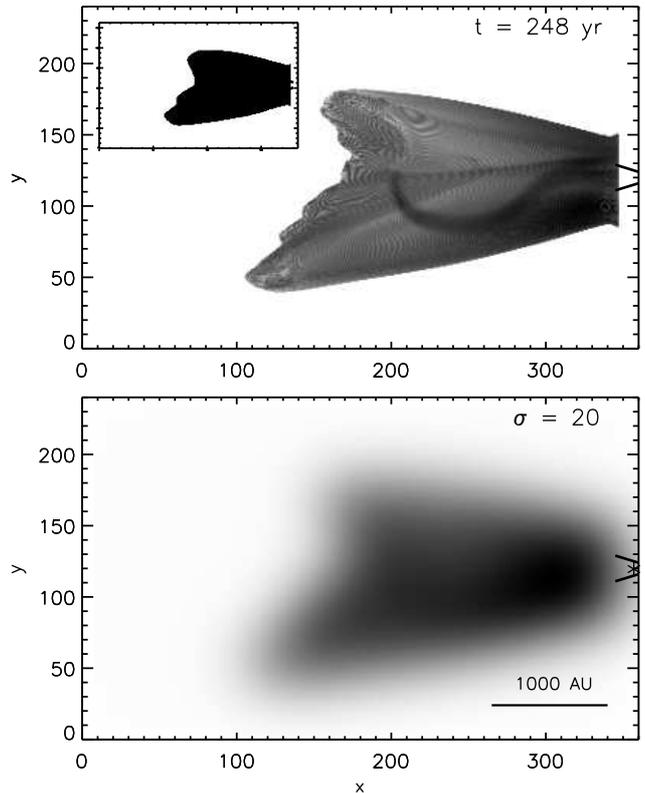
CO data is a few times that derived for the precessing H_2 feature currently prominent. The true age of the bipolar outflow now being observed may thus be much shorter, being driven by fast jets. However, it also seems plausible that a massive outflow has been in existence for a time exceeding 10,000 yr to be consistent with their apparent ubiquity. This suggests that massive stars may also undergo outburst episodes, possibly related to FU Ori type accretion events or merging events.

The observed K-band arcs of emission could arise from vibrationally-excited H_2, scattered continuum emission from stellar object, or emission from warm dust grains. Most likely, the observed emission is a combination of all three processes. In the numerical study, the molecular hydrogen is vibrationally excited only in shocks, being calculated from formula which take into account collisional excitation and collisional and radiative de-excitation. The shocks from which the near-infrared emission originates are J-type of speed exceeding ~ 8 km s^{-1}, capable of heating the gas above ~ 1000 K in gas of density exceeding 10^4 cm^{-3}. As a consequence, along with distortion and projection effects of the shock front, the strongest emission is predicted to occur from the edges of the rim structures

(locations A and B in Fig. 3) whereas the observed emission appears to peak towards the center (the flow axis). The emission from nearer the source, within region C in the simulated image, may also be influenced by stronger extinction. Fluorescent excitation of H_2 and scattering of radiation from the central source thus seems to dominate the observed emission around the flow axis. Narrow-band imaging and polarimetry would be helpful to distinguish between these possibilities.

The observed backward facing curved shock can be understood as a remnant of the initial ring of shocked gas around an inward pointed cone of ambient material trapped within the volume of material swept up by the precessing jet. The ring of shocked gas fragments into numerous bow-shocks and curved filaments, but the head of the inward pointed cone remains visible for some time and points towards the jet source.

Further support for our interpretation of a jet-driven flow comes from the observed elongated feature connecting IRS 1 to the nebulosity. This feature may trace of the most recently ejected material in the precessing jet. It points just towards the southern edge of the most prominent bow-shock like structure, consistent with the idea that the bow represents an inward-pointed cone that has been created by a jet precessing around the cone's surface. The jet of emission from the driving source is not visible in our simulated image, what may well be due to the absence of short period oscillations in the jet. In any case, pulsations tend to decay very rapidly within jets and do not readily produce elongated jet structures. Nevertheless, by changing the cuts in our data to enhance weaker features (insert of Fig. 3), we do indeed find a jet-like structure in the observed direction. It appears to be related to the transverse motion of the precessing jet, which pushes into relatively undisturbed cavity material. In other words, a continuous jet-like structure can be produced due to the interaction between a wandering jet and the cavity walls.

In summary, modeling suggests that the outflow is jet-driven and the jet precesses with a period of ~ 1500 yr. Such a precession period may be triggered by a companion protostar either orbiting within 30–100 AU (i.e. within a 10 $M_\odot$ system with a period of 50–300 yr) and/or in the process of merging.

5. Comparison of IRAS 23151+5912 with other intermediate- and high-mass YSOs and radiative transfer model images

Complex structures are generally detected in the immediate circumstellar environments of intermediate- and high-mass protostars, and IRAS 23151+5912 is no exception. In Fig. 5 we show a mosaic of K-band bispectrum-speckle images from several intermediate- and high-mass protostars that have been observed by our group during the last few years. As illustrated in Fig. 5, different objects display intriguingly different near-infrared morphologies. This is, perhaps, not surprising given the following vital intrinsic sources of influence:

Table 1. Basic data for the six sources discussed in § 5. Note that there is a strong dependence on the poorly known distances. The length scales in AU corresponding to the one arcsecond scale, as indicated by the bars shown in Fig. 5, are equivalent to the distance in parsecs (column 4).

Object	Luminosity [$L_\odot$]	Mass [$M_\odot$]	Distance [pc]
S140 IRS3	3×10^3	8	1000
S140 IRS1	5×10^3	10	1000
Mon R2 IRS 3	1×10^4	10	800
AFGL 2591	2×10^4	12	1000
IRAS 23151	1×10^5	25	5700
K3-50A	2×10^6	30	8700

– the evolving properties of the central radiating source,
– the varying impact and disruption by the jet and/or wind,
– the clumpy small-scale distribution of surrounding material, and
– the configuration of large-scale geometric components.

In addition, the viewing angle is an extrinsic factor which needs to be taken into account before we can relate the structure to the physical cause. With this purpose, we here compare bispectrum speckle images to each other and to radiative transfer simulations.

5.1. Observed infrared morphologies

The relevant properties for the six objects shown in Fig. 5 are listed in Table 1. The major qualitative features are summarised below.

S140 IRS3 is resolved into three point sources and an extended diffuse feature north-east of IRS 3 that displays a remarkable S-shaped structure (Preibisch et al. 2001). This feature is the innermost part of an at least 15″ long structure that extends towards a bow-shock like patch located 90″ away from IRS 3. It is also associated with strong, shock-induced H_2 line emission, indicating a collisional interaction between outflowing material and the ambient medium. The S-shaped structure was successfully reproduced by a model involving a precessing outflow stemming from IRS 3A (the brightest point source in the image).

The brightest feature in the image of **S140 IRS1** is the bright, extended, and very clumpy structure pointing away from the central source, IRS1, towards the southeast, in the same direction as the blue-shifted CO outflow lobe (Schertl et al. 2000, Weigelt et al. 2002a). We interpret this feature as the clumpy inner surface of a partially evacuated cavity which has been excavated by the strong outflow from IRS1. A system of three arc-like structures to the north-east could be produced by a precessing jet interacting with cavity walls. The systematic positional offsets of their bow-shaped tips then correspond to the successive sites of jet impact. These results provide direct
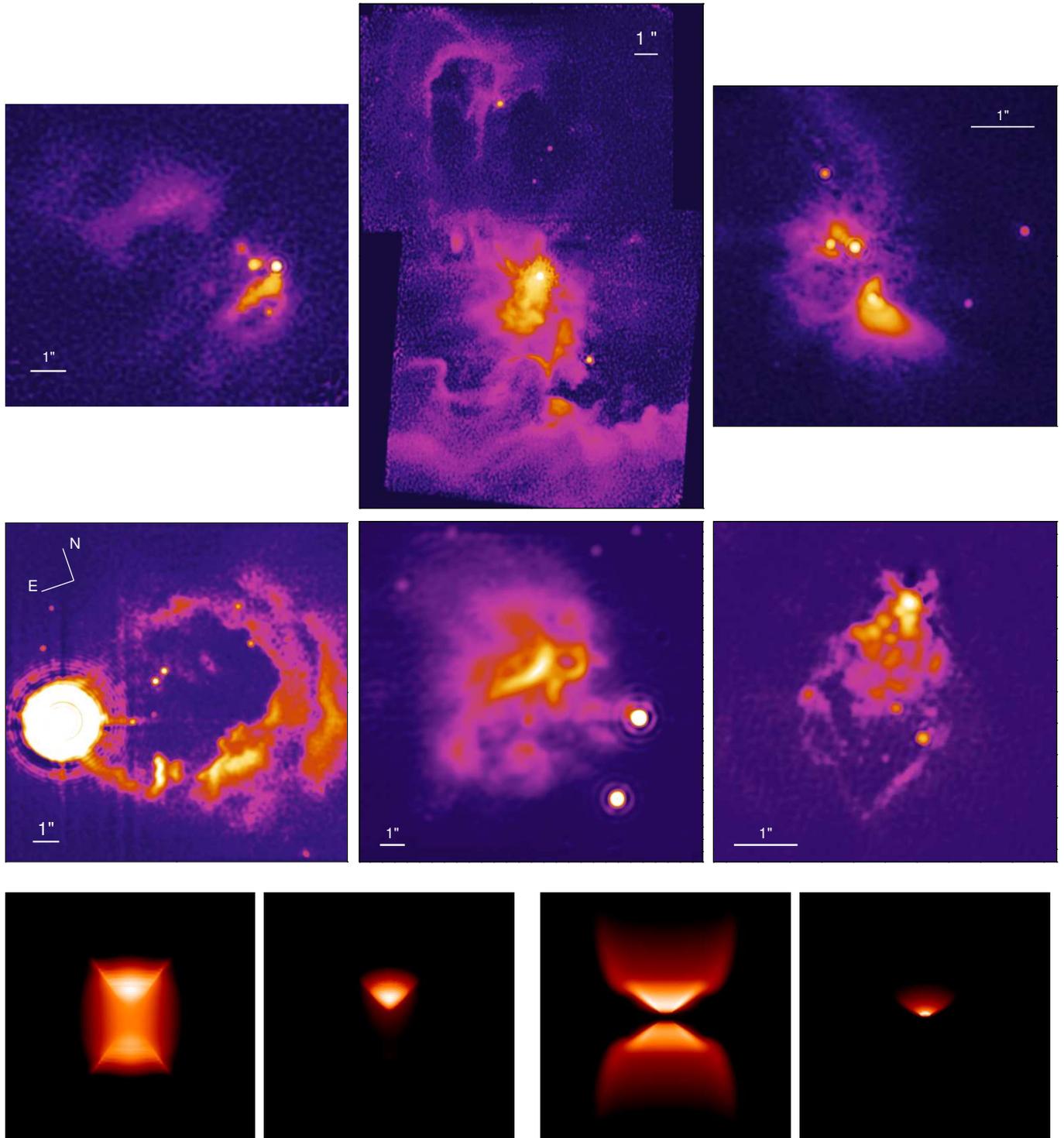
Fig. 5. Comparison of K'-band images from bispectrum speckle interferometry of several intermediate- and high-mass YSOs to radiation transfer simulations.

Upper two rows: Pseudocolor representations of several images. The objects are arranged by increasing estimated luminosity (or mass) of the YSO. The first row displays S140 IRS3, S140 IRS1, and Mon R2 IRS 3 (from left to right). The second row shows AFGL 2591, IRAS 23151+5912, and K3-50 A. For details and references see text. In all images north is up, and east is to the left. The length scales in AU corresponding to the one arcsecond bars shown in the images are given by the numbers in Table 1 col. 4. Lower row: simulated K-band images derived from 2D radiative transfer calculations. The two left images correspond to a spherical envelope model with cone-like cavities (Model A), seen under inclination angles of $i = 85°$ and $i = 60°$. The two right images are from a model of a Keplerian disk embedded in a spherical halo with polar outflow cavities (Model B), again for inclination angles of $i = 85°$ and $i = 60°$. Each image shows a 1250 AU $\times$ 1250 AU region. For details of the models see the text.

evidence for the existence of two distinct bipolar outflow systems driven simultaneously from IRS 1.

The speckle images of **Mon R2 IRS 3** reveal a close triple system surrounded by diffuse nebulosity (Preibisch et al. 2002). A prominent bipolar nebula surrounds IRS 3 A (the brightest point source just beneath the center of the image). IRS 3 B (the second brightest point source, just above the center of the image) shows a remarkable jet-like emission feature pointing towards the north-east.

The **AFGL 2591** image displays a well-defined conical structure with a bright infrared source at the apex (Preibisch et al. 2003). Several loops of nebulosity are clearly seen, which suggest that shock waves driven by discrete outbursts have swept through the cavity.

The image of the ultracompact H II region **K3-50A** resolves the central $1'' \times 1''$ region into at least 7 point-like objects (Hofmann et al. 2004). The cone-shaped nebulosity extending to the south contains considerable fine-structure. The brightest K'-band source is located exactly at the tip of the cone. The nebula also shows several arcs. The orientation of its main axis corresponds to the direction of the CO outflow from K3-50A.

5.2. Radiative transfer simulations

We have performed a number of radiation transfer simulations of YSOs surrounded by envelopes and/or disks in order to better recognize the physical structure behind the features in the speckle images. We applied the 2D radiation transfer code described in Sonnhalter et al. (1995). In this code, the distribution of dust temperatures and radiation intensities in an axially symmetric, dusty circumstellar environment around a central radiation source is calculated within the framework of the flux-limited diffusion approximation (Levermore & Pomraning 1981).

The equations are discretized on a quadratic, equally spaced grid. To improve resolution and convergence, a system of 5 nested grids with decreasing grid spacing is used. The differential equations for the radiation field are iterated together with the temperature equations until a self-consistent equilibrium configuration is reached. After the determination of the dust temperatures for a multi-component dust model, a ray-tracing procedure is used to calculate intensity maps for the appearance of the central object and its circumstellar environment at varying inclinations for selected frequencies. A detailed description of the code is given in Sonnhalter et al. (1995).

In our simulations we assume a luminosity of $20\,000\,L_\odot$ and an effective temperature of $30\,000$ K for the central source. The dust model is described in the Appendix. It was derived from Preibisch et al. (1993), and was constructed to reproduce the dust properties in dense molecular clouds.

We consider two different models for the density distribution of the circumstellar material. Model A assumes that the central source is embedded in a dusty *envelope* with a radial power-law density distribution that is bounded by a Fermi-type function at an outer radius of 3.5×10^{15} cm (233 AU). The cavities are simulated as a pair of cones with their tips at the position of the central star, in which the density is 1000 times smaller than in the other parts of the envelope at the same radial distance from the center. The model details are provided in the Appendix.

Model B assumes a geometrically thick Keplerian *disk*, which is embedded in a spherical halo that has wind-blown cavities along the rotational axis. We employ an analytical model for a Keplerian disk, which is expected if the central potential of the star is the dominating gravitational potential in the disk. Again, the details are provided in the Appendix.

Simulated K-band images for the two models with different inclination angles are shown in the lower row of Fig. 5. The contrast range displayed in the images is 4 orders of magnitude. For high inclination angles ($i = 85°$, i.e. nearly edge on) the direct view towards the central source is blocked, and the dominant features in the simulated images are scattering lobes above and below the disk or torus plane. For low inclination angles ($i = 60°$), the observer is able to "look through" the less dense regions of the cavities towards the hottest and, therefore, bright central regions. Hence, the extension of the scattered light is relatively small for a given contrast ratio. Note that these model images should only be compared to the large scale morphology in the observed images. The small-scale clumpiness and bow-shocks captured in the speckle images cannot be simulated in our 2D radiative transfer model.

5.3. Comparison of observed morphologies and simulations

A common feature in the menagerie of images is diffuse emission extending from the central point-like source with a fan-shaped morphology. The detailed shape and structure of the diffuse emission varies strongly from object to object. A critical factor in the appearance of the structures is the inclination between the outflow/cavity axis and the line-of-sight. In fact, the radiation transfer simulations described below demonstrate that the cone of the bipolar cavity oriented towards us appears very bright for moderate or low inclination angles ($i \lesssim 75°$). The opposite cone is considerably fainter or completely invisible because it is oriented away from us and hidden by circumstellar extinction. Objects with low inclination angles are thus suggested to be S140 IRS 1, K3-50A, and IRAS 23151+5912. In systems with high inclination angles ($i \gtrsim 75°$), a more symmetric morphology is expected. A good example in our sample is Mon R2 IRS 3A where, in addition to the bright nebulosity toward the south, fainter nebulosity can be seen north of the point source, resembling a bipolar reflection nebulosity.

The observations indicate that a second difference is related to the intrinsic asymmetry of the cavity structure itself. In some objects the shape of the cavity ap-

pears highly symmetric (e.g., S140 IRS1, AFGL 2591, K3-50A), while other objects show remarkable asymmetry (e.g., S140 IRS3).

A third major difference is the relative amount of reflected light and H_2 shock emission. In S140 IRS1 and Mon R2 IRS 3A, the infrared morphology is strongly dominated by light reflected from the inner cavity walls. In other objects we observe emission from shocked material in the vicinity of the jets (e.g., the north-eastern jet from S140 IRS3; see Preibisch et al. 2001) or outflowing shock waves seen in reflected light, such as the loops in AFGL 2591.

Can we distinguish a jet-driven outflow model from a wind-driven model? The jet-driven outflow model predicts highly collimated axial flows, while the wind-driven model predicts wide-angle shells and loops. Many of the YSOs in our sample suggest both kinds of outflow activities. The stellar wind is expected to play an increasingly important role in driving the outflows with increasing mass of the YSO. Furthermore, a wide-angle wind is expected to clear a broader path in the surrounding circumstellar matter than a highly collimated jet. In our sample of intermediate-to-high mass YSOs we see some indication that the cavity opening angle increases with increasing luminosity of the central YSO, tentatively supporting this suggestion. However, jet precession and multiple outflows also clearly act to broaden cavities in the two lower mass examples, making any relationship less obvious.

Comparing the observed images to the radiative transfer simulations, we find that the objects showing triangular-shaped morphologies with rather straight walls (AFGL 2591, IRAS 23151+5912, and K 3-50 A; second row in Fig. 5) are quite well reproduced with Model A, the inclined "envelope with cavity" model. For S140 IRS3 and S140 IRS1 (upper row in Fig. 5), the very elongated nebulosities may indicate a very small cavity opening angle. The observed bipolar structure around Mon R2 IRS 3 A (Fig. 5 c), on the other hand, appears reminiscent of the disk model B, seen under a rather high inclination angle.

To summarize, the large-scale features observed in the speckle images can be understood in the frame of simple disk or envelope plus cavity models, whereas the small scale structure depends on additional factors such as clumpiness of the circumstellar material and the presence of shock waves.

6. Summary and Conclusions

A bispectrum speckle image of the massive protostellar object IRAS 23151+5912 reveals complex structures with several arcs in the infrared nebulosity to the north-east of the driving source. The nebulosity is coincident with the blue-shifted CO outflow, which is consistent with a model in which the red-shifted lobe of the outflow is hidden from view in the near-IR through intervening extinction. The general morphology of the arcs in the nebulosity can be reproduced by a model assuming that the outflow is driven by a precessing jet. Our findings constitute another ex-

ample for an apparently jet-driven outflow from a massive protostar and support the assumption of a common mechanism for the formation of outflows from protostars of all masses. We have performed new simulations of 3D hydrodynamic precessing jets and 2D radiative transfer in cavities. On comparison to a set of speckle images, we conclude that the inner infrared structures of high-mass stars are strongly influenced by the orientation and symmetry of the bipolar cavity, as well as the relative strength of shocked and reflected emission components.

Finally, we can speculate about the reason for the precession of the outflow from IRAS 23151+5912. One possible explanation might be that the outflow source is a member of a close (unresolved in our images) binary system where the rotational axis of the star driving the outflow is misaligned with the orbital plane of the binary (see, e.g., Terquem et al. 1999; Bate et al. 2000). Other possibilities include anisotropic accretion events that altered the angular momentum vector of the disk, or radiation-induced warping of the disk, as discussed by Shepherd et al. (2000).

References

Akeson, R.L., Walker, C.H., Wood, K., et al., 2005, ApJ 622, 440

Bate M.R., Bonnell I.A., Clarke C.J., et al., 2000, MNRAS 317,773

Beuther H., Schilke P., Menten K.M., Motte F., Sridharan T.K., Wyrowski F. 2002a, ApJ 566,945

Beuther H., Schilke P., Sridharan T.K., Menten K.M., Walmsley C.M., Wyrowski F. 2002b, A&A 383,892

Beuther H., Walsh A., Schilke P., Sridharan T.K., Menten K.M., Wyrowski F., 2002c, A&A 390,289

Brandner, W., Sheppard, S., Zinnecker, H., et al. 2000, A&A 364,L13

Campbell, M.F., Kassis, M., Adams, J.D., Hora, J.L., Deutsch, L.K. 2003, AAS Meeting 202, #28.05

Chen, X.P., Yao, Y.Q., 2004, Chin. J. Astron. Astrophys, 3, 284

Churchwell E., 2000, in The Origin of Stars and Planetary Systems, eds. C.J. Lada & N.D. Kylafis, (Kluwer Academic Press)

Devine D., Bally J., Reipurth B., Schepherd D., Watson A. 1999, AJ 117,2919

Dougados, C., Cabrit, S., Lavalley, C., Menard, F. 2000, A&A 357, L61

Eisner, J.A., Hillenbrand, L.A., White, R. J., Akeson, R.L., Sargent, A.I., 2005, ApJ 623, 952

Felli, M., Palagi, F., Tofani, G., 1992, A&A 255, 293

Hodapp, K.-W. 1994, ApJS 94,615

Hofmann, K.-H., Balega, Y., Preibisch, Th., Weigelt, G. 2004, A&A 417,981

Labeyrie A. 1970, A&A 6,85

Leinert, Ch., van Boekel, R., Waters, L. B. F. M., et al. 2004, A&A, 423, 537

Levermore, C.D. & Pomraning, G.C., 1981, ApJ 248, 321

Lohmann, A.W., Weigelt, G., Wirnitzer, B. 1983, Appl. Opt. 22,4028

Millan-Gabet, R., Monnier, J.D. 2002, ApJ 580,L167

Preibisch, Th., Ossenkopf, V., Yorke, H.W., Henning, Th. 1993, A&A 279,577

Preibisch, Th., Balega, Y.Y., Schertl, D., Smith, M.D., Weigelt, G. 2001, A&A 378,539

Preibisch, Th., Balega, Y., Schertl, D., Weigelt, G. 2002, A&A 392,945

Preibisch, Th., Balega, Y., Schertl, D., Weigelt, G. 2003, A&A 412,735

Reipurth, B., & Bally, J. 2001, ARAA 39,403

Rosen A., Smith M.D. 2004a, A&A 413,593

Rosen, A., Smith, M. D. 2004b, MNRAS, 347, 1097

Scalise, E., Rodriguez, L.F., Mendoza-Torres, E., 1989, A&A 221, 105

Schertl, D., Balega, Y., Hannemann, T., et al. 2000, A&A 361,L29

Shepherd, D.S., Yu, K.C., Bally, J., Testi, L. 2000, ApJ 535,833

Smith, M. D., & Rosen, A. 2005, MNRAS, 357, 579

Sonnhalter, C., Preibisch, Th., Yorke, H.W. 1995, A&A 299,545

Sridharan T.K., Beuther H., Schilke P., Menten K.M., Wyrowski F. 2002, ApJ 566,931

Stapelfeldt, K.R., Krist, J.E., Menard, F., et al. 1998, ApJ 502,L65

Terquem C., Eislöffel J., Papaloizou J.C.B., Nelson R.P., 1999, ApJ 512,L131

Tofani, G., Felli, M., Taylor, G.B., Hunter, T.R., 1995, A&A 112, 299

Weigelt, G. 1977, Opt Commun. 21,55

Weigelt, G., & Wirnitzer, B. 1983, Optics Letters 8,389

Weigelt, G., Preibisch, Th., Schertl, D., Balega, Y.Y., Smith, M.D. 2002a, A&A 381,905

Weigelt, G., Balega, Y., Hofmann, K.-H., Preibisch, Th. 2002, 2002b, A&A 392,937

Wouterloot J.G.A., Walmsley C.M. 1986, A&A 168,237

Wouterloot J.G.A., Henkel C., Walmsley C.M. 1989, A&A 215,131

Appendix A: The radiative transfer model

The dust model consists of small amorphous carbon grains and large silicate grains and assumes that the silicate grains are coated with a mantle of "dirty ice" if their temperature is below 125 K. The radii a of the grains obey a power law distribution of the form $n(a) \propto a^{-3.5}$, where we assume that the carbon grain radii range from 7 nm to 30 nm and the silicate radii from 40 nm to 1 μm. The ratio between the radii of ice-coated and uncoated silicate grains is 1.145. The "dirty ice" consists of a 3:1 (volume) mixture of H_2O and NH_3, which

is polluted with 10 % carbon particles. When the ice coatings sublimate, the carbon particles are set free and a "naked" silicate grain remains. The sublimation temperatures of the silicate and carbon particles are taken to be 1500 K. The destruction of grains through sublimation is simulated by setting the number density of the grains to zero, if the temperature of a particular grain component calculated simultaneously with the radiation field is above the sublimation temperature. The inner boundary of the dusty environment around the central source is therefore given by the point of dust sublimation.

The envelope density in Model A is

$$\rho_{\text{envelope}} = \begin{cases} \rho_{\text{halo}} & \text{for } z/r < 1.5 \\ \frac{1}{1000} \times \rho_{\text{halo}} & \text{for } z/r \geq 1.5 \end{cases} \quad \text{(A.1)}$$

with

$$\rho_{\text{halo}} = \rho_0 \times \left(\frac{r}{r_0}\right)^{-1.25} \times \left(1 + e^{(r - r_0)/\alpha}\right)^{-1} \quad \text{(A.2)}$$

where ρ_0 is the density of the envelope at a characteristic radius $r_0 = 3.5 \times 10^{15}$ cm = 233 AU and $\alpha = 0.12 \times r_0$. The full opening angle of the cavities is $67°$.

The total density in the disk Model B can be written as

$$\begin{aligned} \varrho(z,r) = \ & \varrho_{\text{disk}} \left(1 + e^{(r - r_s)/\alpha}\right)^{-1} \\ & + \ \varrho_{\text{halo}} \left[\left(1 + e^{-(r - r_s)/\alpha}\right) \right. \\ & \left. \times \left(1 + e^{(z - z_h)\cos\theta/\alpha}\right)\right]^{-1}. \end{aligned} \quad \text{(A.3)}$$

The parameters r_s and $z_s = h\,r_s$ fix the radius and height of the disk while α determines the width of the transition zone of the Fermi-type functions. The halo density ϱ_{halo} is given by

$$\varrho_{\text{halo}} = \varrho_s \frac{r_s^2}{r^2 + z^2}, \quad \text{(A.4)}$$

and ϱ_s is the density of the disk at $r = r_s$ and $z = 0$. Points with $z > z_h$ lie within the cavities. They are modeled by

$$z_h = z_s \left(\frac{r}{r_s}\right)^4, \quad \text{(A.5)}$$

The slope of z_h fixes θ by

$$\cos\theta = \left(1 + \left(4\,\frac{z_h}{r}\right)^2\right)^{-1/2}. \quad \text{(A.6)}$$

For the density of the disk ϱ_{disk} we take an analytical model for a Keplerian disk, assuming that the central potential of the star is the dominating gravitational potential in the disk:

$$\varrho_{\text{disk}} = \varrho_s \left(\frac{r_s}{r}\right)^{15/8} e^{-\pi/4 \left(z/z_s (r_s/r)^{9/8}\right)^2}. \quad \text{(A.7)}$$

We fixed the parameters to $r_s = 3.5 \times 10^{15}$ cm = 233 AU, $h = 0.4$, and $\alpha = 0.1 \times r_0$.